Engineering Science & Technology
https://ojs.wiserpub.com/index.php/EST/

Research Article

A One-Dimensional Model for Polypropylene Fiber Formation in Spunbonding Based on Airflow-Coupled Thermally Dominated Crystallization

Behrang Mohajer, Amirmehdi Salehi, Amirjalal Jalali, Chul B. Park*, Markus Bussmann

Microcellular Plastics Manufacturing Laboratory (MPML), Department of Mechanical and Industrial Engineering, University of Toronto, Toronto, ON, Canada
E-mail: chul.park@utoronto.ca

Received: 25 March 2026; **Revised:** 22 May 2026; **Accepted:** 23 June 2026

Abstract: We propose a practical semi-empirical one-Dimensional (1D) elongational rheology and crystallization model for fiber formation within the spunbonding drawing region. The model predicts fiber diameter variations resulting from feed rate and drawing variations, which are common in the spunbonding process. To simplify the simulation of the polymeric phase, we introduce a method that reduces the need for extensive experimental fitting by a series of rapid simulations, among which the fitting case is selected by comparing the final fiber diameters. Fitting is based solely on the final fiber diameter at the conveyor, which is more accessible than the calorimetric or in-situ crystallization data required by conventional methods. This process consists of two steps: (1) performing a detailed Computational Fluid Dynamics (CFD) simulation to model the airflow within a large domain of the drawing region and determine the airflow being drawn from the surroundings toward the spinline, and (2) using the resulting air velocity profile as a boundary condition for our 1D fiber formation model. Alternatively, the air velocity in step (1) can be measured experimentally at various locations and incorporated as a boundary condition, enhancing the method's generalizability across different drafter geometries and operating conditions. Inspired by the Kanai et al. correlation framework, our 1D model in step (2) integrates heat transfer rates and extensional-thickening behavior within a thermally dominated crystallization framework: the relative crystallinity $\xi(T)$ is expressed as a function of temperature alone, and the influence of Flow-Induced Crystallization (FIC) on melt rheology is captured indirectly through G_K. The model relies on a single empirical constant, G_K, requiring only one experimental fitting parameter per operating regime. G_K is not a material constant but a system-dependent effective parameter—equal to the logarithm of the total viscosity amplification from die to conveyor—whose value varies with throughput and drawing conditions. Since fiber Reynolds numbers remain of order unity, the airflow and fiber phases are one-way coupled; this allows a detailed air velocity profile to serve as a boundary condition, shifting computational complexity from crystallization kinetics to the more tractable airflow dynamics. We conducted a series of experiments using cryogenic Nitrogen (LN_2) to freeze molten fiber samples at various positions between the die and conveyor of a lab-scale spunbonding machine for comparison with the simulated data. We also performed X-Ray Diffraction (XRD) analysis of crystallized samples, which provided further insight into G_K, the effective crystallization index introduced in this study. The model reproduces measured diameter profiles across all tested feed and draw conditions, with the fitted G_K values reflecting the coupled influence of throughput and drawing force on effective crystallization rate.

DOI: https://doi.org/10.37256/est.7220269944

***Keywords*:** flow-induced crystallization, spunbonding, elongational viscosity, airflow coupling, one-dimensional modeling, openFOAM, shear drag

1. Introduction

Spunbonding [1] is a well-established industrial method for producing polymeric nonwoven textiles, widely utilized in applications such as filtration masks, diapers, and liquid absorbents. Figure 1 presents a schematic of the spunbonding process. This method shares similarities with melt-spinning [2]-[4] and melt-blowing [5]-[8].

Spunbonded products are notably thin yet possess significant mechanical strength, making them suitable for medical filtration, as demonstrated during the Coronavirus Disease 2019 (COVID-19) pandemic, as well as for nano-fibrillation products [9], [10]. The spunbonding process has gained increased attention in recent years [11], [12], although substantial scope for advancement remains.

We focus on the drawing region of the spunbonding process. This region begins immediately below the die, where numerous fibers exit the die holes into the ambient air. In this region, fibers are stretched, thinned, and drawn into the drafter before being deposited onto a conveyor belt (Figure 1). Crystallization occurs along the drawing region and is a critical process that significantly influences the product properties and performance. Among the various mechanisms governing crystallization, Flow-Induced Crystallization (FIC) is a key phenomenon in spunbonding, where the dynamics of polymer flow affect the nucleation and growth of crystalline structures [13], [14]. The crystals grow aligned with the flow direction, as Figure 2 depicts. This alters the melt characteristics, in contrast to quiescent crystallization. Moreover, directionally strengthened fibers enhance the applications of spunbonding products [15], [16].

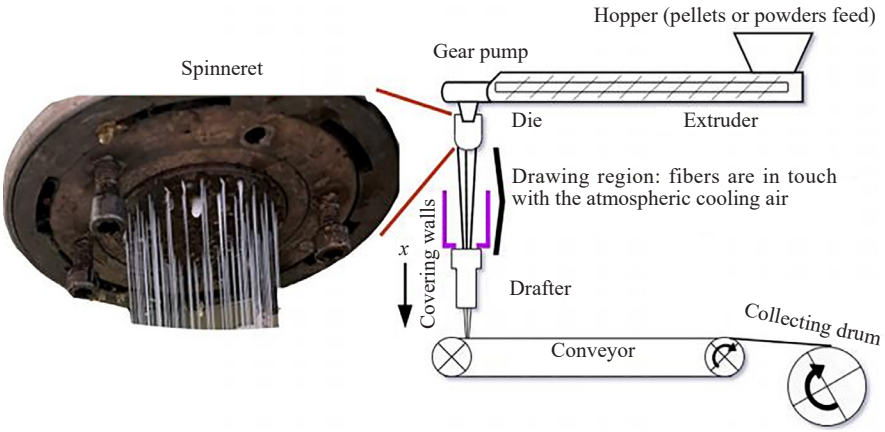

Figure 1. Spunbonding process and the spinneret

While the literature extensively explores fiber formation in melt-spinning [17]-[20] and melt-blowing [21]-[24], studies on spunbonding are relatively scarce. Initial research on spunbonding began in the 1960s, with studies focusing on the emerging drawing region, e.g., [25].

A key feature that distinguishes spunbonding from melt-spinning and melt-blowing is the extended duration over which the drag force (F_{drag}) is exerted while the fiber undergoes convective cooling. Throughout the drawing region, air flows along the fiber, accelerating in the same direction as the fiber. This persistent shear drag thins the fiber gradually without causing breakage.

The heat transfer mechanism in spunbonding is distinct from that in melt-spinning due to the co-current airflow induced by the drafter along the spinline. Bond [18] underscored this difference, which results in slower cooling in spunbonding compared to other spinning processes and thus longer thinning of the polymeric melt. This slower cooling rate allows for a longer stretching time, enhancing further molecular chain reorientation. It is also common practice to enclose the drawing region to focus the co-current airflow, so we installed covering walls in our experiment. Co-current

cooling also occurs in melt-blowing, but the melt transfers heat faster and has a shorter drawing time. Because of this, spunbonded nonwovens possess better filtering and absorbance capability than those produced by melt-spinning and melt-blowing, and the fibers have better directional mechanical properties. This co-current heat transfer mechanism is unique to spunbonding but has been relatively underexplored in the literature [26], [27].

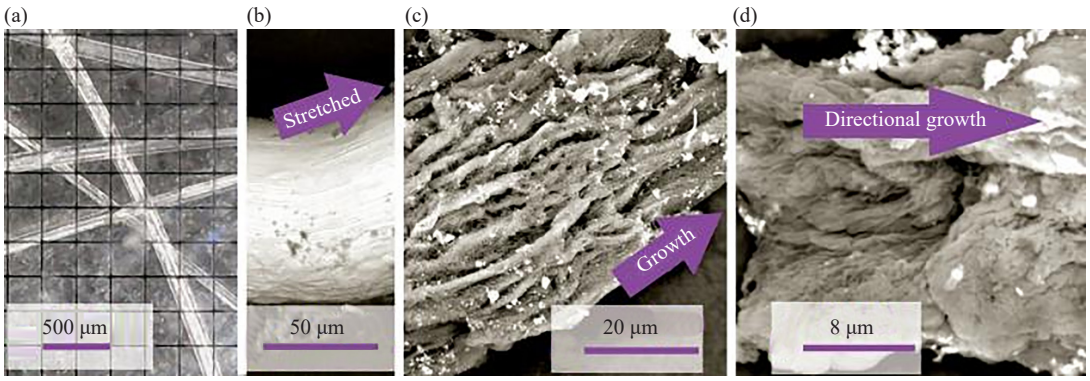

Figure 2. Micrographs of spunbonded Pure Polypropylene (PP) samples. a) Multiple fiber samples on an optical microscope grid. b) Scanning Electron Microscopy (SEM) of a spunbonded fiber demonstrating the stretching effects on the fiber skin. c) SEM view of the fiber with the amorphous phase etched off in boiling Xylene, showing directional crystal growth under elongational strain. d) Image of the crystalline phase at higher resolution

The existing spunbonding literature often attempts to adapt melt-spinning models (e.g., shooting method [17], [27], [29]) or methods similar to those used for melt-blowing deposition (e.g., [29]). Some studies have also employed non-simulation mathematical approaches like machine learning to analyze available experimental data (e.g., [30]-[32]). A comprehensive review of available mathematical approaches for modeling elongational FIC, including empirical, semi-empirical, and molecular-based formulations, is provided in [33], which also motivates the simplified modeling strategy adopted in the present work.

Recent FIC modeling approaches span a wide range of mechanistic complexity. Molecular-dynamics simulations [34] illuminate the multistep nucleation process at the nanoscale but are computationally prohibitive for spinline-length do-mains. Multiphysics crystallization models [35] couple flow, temperature, and kinetic evolution through multiple empirical parameters that require dedicated characterization experiments. Elongational-FIC constitutive models [36], [37] capture strain-rate-dependent nucleation and growth but demand transient rheological datasets not routinely available for process-grade resins. The present model occupies a complementary niche: it sacrifices mechanistic resolution in favor of a single identifiable parameter (G_K) and a precomputed airflow boundary condition, yielding a tractable framework for practical process tuning without multi-parameter fitting.

Several factors have contributed to the limited detailed modeling of the spunbonding drawing region, leading to the predominance of a trial-and-error approach for tuning spunbonding processes:

1. Significant feed material variations due to material grade, impurities, and recycled content.

2. The simultaneous extrusion of tens or hundreds of fibers from the die, which experience varying degrees of convective cooling, stress, and drag forces due to their relative positions and angles. The resulting range of differences is significant and challenging to simulate.

3. Research that favors studying novel blends and composites experimentally with an existing machine, e.g., [38]-[46], rather than the simulation of the process.

4. The complexity of modeling elongational FIC [36], [47], particularly given the high-velocity gradients and severe cooling rate ranges in spunbonding, which existing analytical formulas are ill-suited to handle.

Variations in feed composition and fiber properties pose significant challenges to validate simulation models. Although in-situ sampling techniques have been employed to obtain crystallization data (e.g., [48]), their application is often im-practical for simulating every minor variation in process conditions. As a result, existing models are difficult to apply for routine process tuning under realistic feed and airflow variations, where only limited experimental data are available.

To address these issues, we present a novel 1D model for fiber formation in spunbonding driven by a simulated airflow boundary. While 1D melt models have been developed for similar purposes (e.g., [16], [17], [27], [28], [30], [49]-[51]), the present approach is distinct in its treatment of FIC: rather than solving a coupled FIC model from first principles, a precomputed or experimentally measured air velocity field is used as a boundary condition, enabling a back-calculation of the effective crystallization rate. This decoupled treatment is justified by the multistep, multiscale nature of nucleation [34]. G_K is a lumped parameter encoding the effective crystallization enhancement under extensional flow conditions, capturing nucleation, growth, and orientation effects through its influence on viscosity evolution. It is not a material constant but an operating-condition-dependent effective parameter; however, only one such value is required per operating regime.

While there are existing models for FIC under idealized or specific conditions (e.g., [52]-[56]), they typically rely on empirical correlations that demand complex experiments. In contrast, we present a model with computational implementation and experimental inputs, which can be conveniently applied to various spunbonding machines.

Step 1 obtains the air velocity profile along the drawing region via Computational Fluid Dynamics (CFD) or direct measurement—data that is often overlooked in other models but straightforward to acquire. Step 2 uses this profile as a boundary condition in the 1D fiber simulation, shifting computational complexity from crystallization kinetics to the more tractable airflow dynamics.

In Section 2, we present our algorithm and introduce the computational models for the airflow and the subsequent fiber simulation. The primary focus of this study is the latter, which builds upon the framework developed by Kanai et al. [28], with modifications to incorporate a more detailed representation of the airflow. Next, we present the results and evaluate the model's predictive capabilities by comparing simulation outputs with experimental data obtained from our lab-scale spunbonding apparatus. The present framework also serves as the macroscopic foundation for a subsequent dual-scale simulation of nanofibrillation phenomena within individual fibers, which has been developed and validated using experimental data in our recent work [57].

2. Methodology

In the two computational steps of this study, we first present a three-dimensional CFD model for the airflow. Subsequently, we present a 1D model that captures the transformation of a polymeric melt into a fiber along the spinline with the airflow as the boundary condition.

The process begins with simulating airflow within the spunbonding drawing region, where ambient air is drawn and accelerated along the spinline. The velocity-driven airflow is modeled using CFD within a Computer-Aided Design (CAD) geometry of the spunbonding machine.

Subsequently, the airflow velocity (U_a) obtained from the first step simulation is applied as a boundary condition to the fiber formation model along the spinline (x). The fiber elongation is primarily driven by shear drag, which is computed based on the velocity difference between the fiber (U) and the surrounding U_a.

2.1 *Step 1: airflow simulation in the drawing region*

In this section, we describe the airflow simulation using OpenFOAM-v7® [58]. The CAD geometry of a lab-scale spun-bonding machine was developed using Autodesk Fusion 360 (Autodesk Inc.). The model was subsequently imported into OpenFOAM, where all solid boundaries were defined as no-slip walls. Two airflow simulations were performed using the incompressible simpleFoam solver, employing the k-ε turbulence model to capture the airflow characteristics around the machine geometry. The primary output of each simulation is the axial air velocity distribution, U_a, obtained for two drafter settings along the spinline. The k-ε model was selected because its predictions of the axial air velocity distri-bution along the spinline were validated against Pitot-tube measurements conducted at accessible points in the drawing region [27], [59]. Although the SST k-ω model is generally preferred for wall-bounded flows owing to its improved near-wall treatment, k-ε proved adequate for the present geometry where the region of primary interest—the spinline core—lies well away from the confining walls. Direct Pitot measurements within the narrow drafter interior were not feasible, so a detailed turbulence-model comparison in that zone remains unavailable; the outer-region validation is taken as sufficient justification for the adopted closure.

Since the fibers are very thin, their influence on the surrounding airflow is negligible at the scale of interest, and the airflow can therefore be treated independently of the polymeric phase. The negligible effect of the thin fibers on airflow, the aerodynamic design of the drafter, and its influence on the resulting drawing air velocity field have been investigated in detail in our earlier work [59], which confirms the use of a CFD-derived airflow profile as a boundary condition in the present model.

The fiber formation model operates independently as a post-processing step, with the air velocity U_a boundary condition interpolated where the simulation grid cells do not align perfectly. Alternatively, the second step can be carried out using U_a values experimentally measured at several points along the drawing region, such as with a Pitot tube.

2.2 *Step 2: fiber simulation along the spinline*

The simulation domain begins at the die hole exit. Figure 3 shows the computational mesh grid for a single fiber, which is discretized into cylindrical cells with uniform height (δx) and a dynamically evolving Diameter (D) influenced by the coaxial airflow.

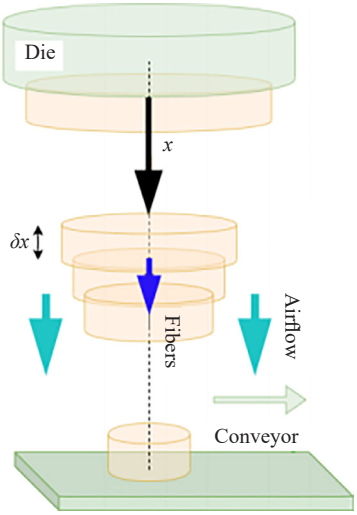

Figure 3. The 1D cylindrical mesh with dynamic diameter in the drawing region. The surrounding air cools and stretches the lateral sides of the cylinders on the spinline

The ratio of drawing length to fiber diameter, $\frac{\text{Drawing region length}}{\text{Die hole diameter}} = \frac{220\text{ cm}}{400\ \mu\text{m}} \approx 5,000$, is large. As a result, the radial momentum and heat transfer within a fiber are negligible in comparison to axial effects at the scale of interest. While a few studies have investigated specific sections of the drawing region where radial distributions may become significant (e.g., [60], [61]), the present analysis deliberately focuses on the dominant axial behavior to enable a tractable and practically deployable 1D model. This 1D assumption is further quantified by a Biot number estimate. Using a representative fiber diameter $D \approx 100$ µm, convective coefficient $h \approx 100$ $Wm^{-2}K^{-1}$, and PP thermal conductivity $k_f \approx 0.2$ $Wm^{-1}K^{-1}$, the lumped-capacitance Biot number for a cylinder evaluates to $B_i = hD/(4\,k_f) \approx 0.013 << 1$, confirming that radial temperature gradients within the fiber are negligible and a 1D (axial-only) treatment is well justified. The present model covers the full spinline from die exit to conveyor; the initial segment near the die, where near-die transient effects and higher local stresses may make radial gradients more pronounced, has been examined separately in a dual-scale study [57]. At substantially higher feed rates or for larger die diameters B_i could approach $O(0.1)$, and this represents a recognized limitation of the 1D assumption.

We solve a steady-state set of 1D transport equations governing mass, momentum, energy, crystallization, and rheology. These equations, summarized in Eq. (1), are implemented in Python 3.8.3 using the NumPy library and iteratively solved until the velocity field converges. The formulation of each transport equation is detailed in Sections 2.2.1 to 2.2.4:

$$\dot{M} = AU\rho = \frac{\pi}{4}D^2 U\rho = \text{ constant } \Rightarrow \frac{dA}{dx} = -\frac{A}{U}\cdot\frac{dU}{dx} \text{ Mass}$$

Rate of momentum change: $^{\Sigma}F = F_{\text{drafter}} + F_{\text{viscous}} + F_{\text{drag}} + F_{\text{weight}} + F_{\text{surface}}$ Momentum

$$\Rightarrow \iint (\rho U)\vec{U}\cdot dA = \iint N_1 \cdot dA + \iint_{\text{side}} F_{\text{drag}} \cdot dA_{\text{lateral}} + \rho g A \delta x$$

Convection heat transfer: $\frac{dT}{dx} = \left(\frac{h\cdot A_{\text{lateral}}}{c_p \cdot \dot{M}}\right)\cdot\left(T - T_a\right);\ T(x=0) = T_{\text{die}}$ Energy (1)

$$\eta(T,\,\xi) = \eta(x) = 3\eta_{\text{shear}}\left(T_{\text{die}}\right)\cdot\exp\left(\frac{E_D}{R}\left[\frac{1}{T(x)} - \frac{1}{T_{\text{die}}}\right]\right)\cdot f\left(x,\ G_K\right) \text{ Rheology}$$

$$\xi = \begin{cases} 0 & T > T_m \\ \dfrac{T_m - T}{T_m - T_g} & T_m > T > T_g \\ 1 & T_g > T \end{cases} \text{ Crystallization.}$$

In the rheology equation, η represents the elongational viscosity, T is the polymeric melt temperature, a function of position (x), T_{die} is the initial melt temperature at the die exit, ξ the relative crystallinity (also a function of x), η_{shear} is the shear viscosity, E_D is the activation energy, R is the universal gas constant, G_K is an empirical index introduced in this study, and f is a numerical function describing rheological behavior in Section 2.2.3.

In the mass equation, $\dot{M}$ is the mass flow rate, A is the fiber cross-sectional area, and ρ is the polymer melt density. In the momentum equation, F_{drafter} represents the external mechanical force applied by the drafter, while F_{viscous} and F_{drag} denote the internal viscous force and the aerodynamic drag on the fiber lateral surface, respectively. The term F_{weight} accounts for the gravitational force acting on the fiber, F_{surface} denotes the surface tension, and N_1 is the first normal stress difference. In the energy equation, h denotes the convective heat transfer coefficient, c_p is the specific heat capacity of the melt, and T_a is the ambient air temperature. Kase and Matsuo's spinning model [2] was adopted for the temperature distribution [16]. In the crystallization equation, T_g, T_m, and ξ are the effective solidification temperature, melting temperature, and the relative crystallinity of the polymer, respectively. We do not attempt to resolve microscopic nucleation or growth kinetics. Instead, we introduce G_K as a lumped effective crystallization rate index that subsumes induction time, nucleation density, growth rate, and flow-orientation effects into a single macroscopic closure. Table 1 lists the property values used in our simulations. We adopted the boundary conditions below for iteration over Eq. (1):

1. Die: $T = T_{\text{die}}$, $D = D_{\text{die}}$, $U = U_{\text{die}}$ obtained from the feed.
2. Surroundings: $T_a = 20$ °C constant and U_a from the air simulation.
3. Conveyor: zero gradients for T, D, and U.

A range of simulations is run for a range of the effective crystallization rate index, G_K. Next, by comparing these predictions with experimental measurements, the user can identify the crystallization rate that best matches their measured fiber diameter. This inferred rate can then be used to predict diameter variations under varying drawing forces and process conditions, providing valuable insight into the coupled effects of cooling efficiency and FIC. Since adjusting the drawing force is a critical task when tuning the drafter—especially in response to subtle changes like material grade variation—having a reliable estimate of the crystallization rate significantly reduces the need for costly and time-consuming trial-and-error experimentation at the industrial scale.

Next, we elaborate on details of Eq. (1) for the solutions of $U(x)$, $D(x)$, $T(x)$, and $\xi(x)$.

Table 1. Detailed values, equations, and boundary conditions for fiber simulation

Property	Explanation	Value or equation
μ_a	Air viscosity	1.81×10^{-5} Pa·s
ρ	PP density	1/(0.000903 T + 1.145) [51]
ρ_a	Air density	1.225 kg/m^3
ξ	Relative crystallinity	Varying between 0-1
A	Cell cross-section	$\frac{\pi}{4}$ D^2
A_{lateral}	Lateral area of a cell	$\pi \cdot D \cdot \delta x$
c_p	Specific heat capacity	0.3669 + 0.00242 T [51]
D_{die}	Die diameter	400 µm
E_D	Activation energy	427,198 J/kg
k_a	Air conductivity	2.550×10^{-4} w/mK
$\dot{M}$	Mass flow rate per hole	(1–2) kg/h ÷ 100 holes
T_a	Air temperature	20 °C
T_{die}	Die temperature	200 °C
T_g	PP effective solidification temperature[1]	50 °C
T_m	PP melting temperature	171 °C
U_a	Air velocity	From air simulation
Air boundary[2]	U	p
Inlet	fixedValues of 50 & 80 m/s	zeroGradient
Far side[3]	zeroGradient	fixedValue of 1 atm
Walls (CAD)	noSlip	zeroGradient

[1]This value is significantly above the exact T_g of isotactic PP (≈ 0 °C). It is used here as an effective solidification temperature, below which the fiber viscosity becomes sufficiently large that further thinning is negligible in the model
[2]The air boundary conditions are illustrated in Figure 4
[3]The far side is the sides of the large surrounding cubes in Figure 4b

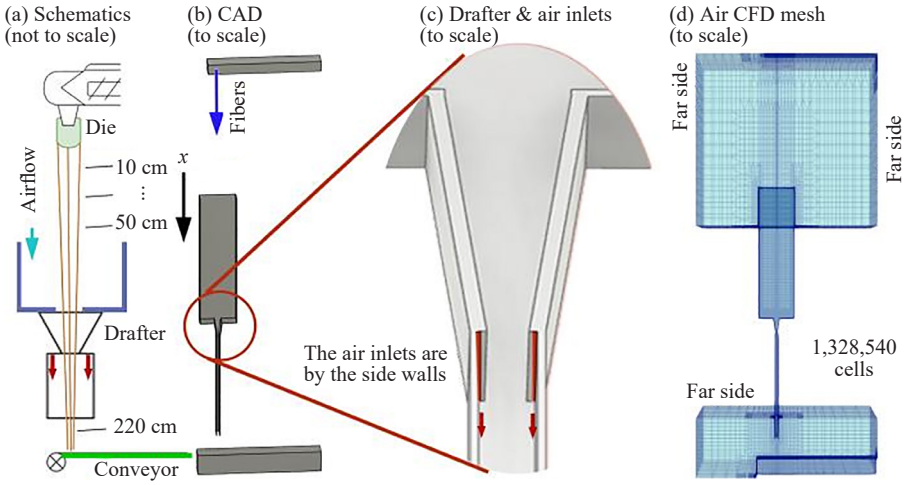

Figure 4. Our lab-scale spunbonding machine and boundary conditions for the airflow simulation: a) schematic of the drawing region; b) CAD geometry, including the die area, the covering walls, the drafter, and the conveyor belt area, with the wall boundary condition applied on all CAD surfaces; c) close-up of the CAD model around the air inlet, comparable to Figure 4; and d) CFD mesh around the CAD geometry to simulate the airflow within the drawing region. This large domain around the spinline allows the pressure to be set to atmospheric far from the fibers

2.2.1 *Momentum conservation equation*

The mechanical drawing force, $F_{drafter}$, is externally applied by the drafter. The direction of F_{drag} varies spatially along the spinline and therefore requires careful treatment. F_{weight} acts in the same direction as the drawing force, aiding the thinning process. Internally, the polymer experiences $F_{viscous}$, which is correlated to N_1 associated with the melt elongational viscosity.

Following standard practice in the literature [2], [18], [51], $F_{surface}$ is neglected and $F_{drafter}$ is merged into the F_{drag} term—both being exerted by the airflow—so that the final momentum balance contains only F_{drag}, $F_{viscous}$, and F_{weight}. Different empirical correlations are applied inside and outside the drafter to account for the distinct flow regimes in each region. Both $F_{drafter}$ and the aerodynamic component of F_{drag} act through the same shear-drag mechanism: the local velocity difference ($U_a - U$) drives a distributed drag force over the fiber lateral surface. Inside the drafter, the covering walls accelerate the co-current air to higher velocities, increasing ($U_a - U$) and therefore the drag; the physical origin of the elevated air velocity does not alter this drag formulation. The direction-preserving form in Eq. (2) captures both regimes continuously.

The simulated airflow around the fiber acts as a boundary condition and contributes to the shear drag force on the fiber lateral surface ($A_{lateral}$). Since the instantaneous fiber diameter remains several orders of magnitude smaller than the characteristic dimensions of the drafter and surrounding airflow domain, and the fiber Reynolds number based on the relative velocity ($U_a - U$) remains on the order of unity (i.e., $Re \sim 1$) or smaller under typical operating conditions, the feedback of the fiber motion on the surrounding airflow is negligible. This justifies a one-way coupling approximation, in which the airflow influences the fiber dynamics but not vice versa.

Spunbonding machines are designed such that, for most of the spinline, $U_a > U$ is maintained with a small difference for slow thinning. The air velocity U_a peaks inside the drafter and then tapers off near the belt. The model also captures possible reversals in the direction of F_{drag} when $U > U_a$ [59]. To capture this behavior, we define the drag force using a direction-preserving form:

$$F_{drag} = \frac{\rho_a}{2} \cdot C_{drag} \cdot A_{lateral} \cdot |U_a - U|(U_a - U)$$

$$C_{drag} = \Psi_1 Re^{-\Psi 2} \tag{2}$$

$$Re = \frac{\rho_a D |U_a - U|}{\mu_a} n$$

where ρ_a is the air density, C_{drag} is the drag coefficient, Re is the Reynolds number, and Ψ_1 and Ψ_2 are empirical coefficients obtained from the experimental work of Chen et al. [62] for two distinct flow regions:

$$C_{drag} = 0.37 Re^{-0.61} \text{ outside of the drafter}$$

$$C_{drag} = 0.91 Re^{-0.61} \text{ within the drafter and covering walls.} \tag{3}$$

These correlations were originally developed for cylindrical fibers subjected to co-current airflows and are valid within the Reynolds number range relevant to spunbonding. Outside this regime, the drag law should be re-evaluated or replaced with alternative correlations.

The two coefficients reflect physically distinct flow environments: $\Psi_1 = 0.91$ was determined by Chen et al. [62] for fibers inside a confined aspirator channel, where wall proximity amplifies the effective surface shear, while $\Psi_1 = 0.37$ applies to the unconfined co-current airflow above the drafter. A sharp switch between the two correlations is applied at the entry of the covering walls.

The complete steady-state 1D momentum balance for the fiber, combining all force terms, gives the following explicit ordinary differential equation for $U(x)$:

$$\frac{d\left(\rho AU^2\right)}{dx}=\frac{d}{dx}\left(\eta A\frac{dU}{dx}\right)+\frac{\rho_a}{2}C_{\text{drag}}\,\pi D\left|U_a-U\right|\left(U_a-U\right)+\rho Ag. \tag{4}$$

Here, the left-hand side is the rate of change of momentum flux (inertia); the first term on the right is the elongational viscous stress gradient, where $N_1 = \eta\ dU/dx$ is the first normal stress difference; the second term is the aerodynamic drag (direction-preserving form, Eq. (2)); and the third term is the fiber weight.

Since the drag force F_{drag} depends on the relative velocity ($U_a - U$), and the fiber velocity U is influenced by F_{drag}, solving the momentum equation requires an iterative approach to achieve convergence.

2.2.2 *Energy conservation equation*

Using the Kase and Matsuo method [2], energy transport is simplified to temperature variation due to convective heat transfer, neglecting work terms, viscous dissipation, and the polymer latent heat [16], [27]. This approximation is justified for thin fibers under moderate elongational stresses, where convective cooling dominates the thermal balance along the spinline.

$$h=f_{\text{heat}}\,(Nu)=\frac{Nu\cdot k_a}{\delta x}. \tag{5}$$

Here, Nu is the Nusselt number, δx is the grid cell height (see Figure 3), and k_a is the air thermal conductivity. The empirical correlation for the Nusselt number in melt spinning is given by [2]:

$$Nu=0.42\left(Re_{\parallel}^2+64Re_{\perp}^2\right)^{0.167}. \tag{6}$$

In Eq. (6), $Re_{\parallel}$ denotes the Reynolds number associated with the air velocity component $U_{a,x}$ parallel to the spinline direction. The perpendicular component, $Re_{\perp}$, is notably more potent, with the multiplier of 64 in Eq. (6), but is null in spunbonding because the radial and polar velocities are zero ($U_{a,r} = U_{a,\phi} = 0$). A survey of Nusselt number correlations for melt spinning and related fiber processes, including several more recent proposals, is provided in [17] (Table 3.2 therein); under the present conditions of purely parallel co-current flow these alternatives reduce to forms comparable to the Kase and Matsuo correlation. Setting $Re_{\perp} = 0$ is maintained intentionally: the covering walls of the drafter suppress transverse airflow, keeping Nu small and thereby prolonging the crystallization window for gradual fiber solidification.

2.2.3 *Rheology equation*

Several models exist for constitutive rheology [63], but using complex constitutive correlations with several fitting param-eters for feed variations can be challenging, even without considering temperature changes, and is further complicated in spunbonding by severe cooling and FIC. Therefore, there are strong incentives to simplify models where FIC is significant (e.g., [64]-[66]). This approach is commonly used in fiber formation (e.g., [29], [33], [49], [56]), as it is easier to estimate the relative crystallinity using only temperature, $\xi(T)$, and to compute T using only convection heat transfer.

Kanai et al.'s model [28] is a notable example. They neglected the extensional thickening effects due to the strain rate compared to crystallization and thus used Eq. (7):

$$\eta(T,\,\xi)=3\eta_{\text{shear}}\,\left(T_{\text{ref}}\right)\cdot\exp\left(\frac{E_D}{R}\left[\frac{1}{T}-\frac{1}{T_{\text{ref}}}\right]\right)\cdot\exp(K\cdot\xi)$$

$$\frac{dU}{dx}=\frac{F_{\text{viscous}}}{\eta A}=\frac{N_1}{\eta} \tag{7}$$

where η is estimated using Trouton's ratio of three, with an Arrhenius-type temperature dependence of viscosity at a reference temperature (T_{ref}). In their correlation, the only experimental coefficient is the rising index K, where $K = 1$ indicates Pure Polypropylene (PP) melt in their study. K decreases with the dosage of low-tacticity PP blended with high-tacticity PP, such that delayed strain-hardening allows molecular chains to reorient further within the melt, resulting in higher mechanical strength of thinner fibers. Kanai et al. used quiescent differential scanning calorimeter data to roughly estimate K in the range of 0.8-1.0 for different dosages, which opens a significant opportunity for further experimental research. They ignored the induction time, die swell, and radial distribution of velocity. The use of Trouton's ratio of three in Eq. (7) is a Newtonian approximation for relating extensional to shear viscosity. For a PP melt at the processing temperatures considered here (above 180 °C), the departure from this ratio under moderate extensional rates is modest [37], and the associated uncertainty is effectively absorbed into the calibrated value of G_K. A more detailed treatment of extensional rheology under spunbonding-relevant deformation rates is provided in [57].

Following their approach, we adopt a similar exponent coefficient G_K, together with a numerical function f and the temperature distribution from the simplified Kase and Matsuo model [2], [16], in Eq. (1)-Rheology, where f is the mathematical representation of the exponential increase in η with G_K. In contrast to Kanai et al.'s direct exponential $\exp(K \cdot \xi)$, here f is implemented as a geometric series over the mesh cells (Eq. (8)), distributing the viscosity growth monotonically without requiring ξ as an explicit input. In this formulation, crystallization is modeled through a rapid increase in viscosity, and hence the faster $f(G_K)$ increases, the faster crystallization effectively occurs; we therefore tune the FIC effect using f.

The only empirical coefficient, G_K, is not merely a material constant. It is an effective crystallization index that depends on both material properties and the local thermo-mechanical history. While Kanai's K is primarily material-dependent, G_K is system-dependent, reflecting the specific aerodynamic and thermal conditions of the machine. Its value therefore varies with feed rate and draw conditions; however, once identified for a given operating regime, it enables prediction of diameter variations within that regime without further experimental fitting.

We used a NumPy geometric series for the function f that distributes the value from η_{die} to $\eta_{die} \times \text{numpy.exp}(G_K)$ geometrically across all mesh cells. This formulation enforces monotonic viscosity growth consistent with crystallization progression while avoiding additional fitting parameters:

$$f(x, G_K) = \text{numpy.geomspace}(\eta_{die}, \eta_{die} \times \text{numpy.exp}(G_K), \text{mesh number}). \tag{8}$$

Since f distributes η from η_{die} to $\eta_{die} \cdot \exp(G_K)$, the final viscosity at the conveyor is $\eta_{conveyor} = \eta_{die} \cdot \exp(G_K)$. This gives G_K an explicit mechanical interpretation as the logarithm of the total viscosity amplification factor due to flow-induced structure formation:

$$G_K = \ln\left(\frac{\eta_{\text{conveyor}}}{\eta_{\text{die}}}\right)_{\text{FIC}}. \tag{9}$$

This logarithmic measure integrates the combined effects of molecular orientation, nucleation, and crystal growth over the full thermal and flow history of the spinline, giving G_K a clear mechanical meaning as the integrated strengthening effect of flow-induced structure formation.

2.2.4 *Crystallization equation*

The melt viscosity both affects and is affected by the relative crystallinity, defined as:

$$\xi(T) = \frac{\Theta(T)}{\Theta_\infty} \tag{10}$$

where $\Theta(T)$ represents the mass fraction of the crystalline phase within the semi-crystalline polymeric structure at temperature T, and Θ_∞ corresponds to the value when all phase transitions have fully concluded after a sufficiently long time.

Rather than resolving microscopic nucleation and crystal growth kinetics explicitly, we introduce a reduced-order

crystallization law in which ξ is expressed solely as a function of temperature:

$$\xi = \begin{cases} 0 & T > T_m \\ \dfrac{T_m - T}{T_m - T_g} & T_m > T > T_g \\ 1 & T < T_g \end{cases}. \tag{11}$$

This formulation assumes that crystallization initiates at the melting temperature T_m, and the fiber is considered solidified at the effective solidification temperature T_g, below which molecular mobility is insufficient to sustain further thinning. Crystallization may continue below T_g, but this is outside the scope of the present model. Although this representation neglects explicit time-dependent induction and growth kinetics, it is appropriate under the high cooling rates and large thermal gradients characteristic of spunbonding, where thermal history dominates crystallization progression. The effect of induction time and growth kinetics is implicitly absorbed into the fitted value of G_K, which affects both the onset and the slope of viscosity growth along the spinline. Spunbonding can exhibit finite induction times, but the present experiments indicate that their macroscopic effect is negligible under the operating conditions considered here. The 2 kg/h half-draw condition is the borderline case: the Deborah number estimate of $De \approx 0.8$ for this condition (see Section 4) indicates that crystallization and flow timescales are of comparable magnitude, consistent with a plausible finite induction time. Under these conditions—lower extensional stress and slower cooling relative to the full-draw case—the present model may underestimate the onset of crystallization, which is also reflected in the low fitted value of $G_K = 0.5$. An offline Differential Scanning Calorimetry (DSC) measurement under controlled cooling rates representative of this condition would enable a more definitive assessment and is identified as a direction for future work.

Accordingly, $\xi(T)$ should be interpreted as an effective macroscopic crystallinity coordinate rather than a microscopic kinetic variable. This reduced-order closure enables a tractable coupling between thermal history, viscosity evolution, and fiber thinning, while retaining only a single empirical crystallization parameter.

It is important to note that the present crystallization model is thermally dominated: ξ depends on temperature alone and carries no explicit dependence on strain rate, stress, or molecular orientation. The influence of extensional flow on crystallization is captured indirectly through G_K, which amplifies the melt viscosity in proportion to the effective crystallization extent. More complete formulations that incorporate flow-dependent crystallization kinetics—including strain-rate-dependent and stress-dependent nucleation models—are reviewed in [33]. The simplified thermally dominated closure adopted here is well-suited for the present operating conditions, where the high cooling rates and strong ther-mal gradients characteristic of spunbonding render thermal history the primary driver of crystallization progression, as confirmed by the experimental validation in Section 4.

3. Experimental setup and sampling with the lab-scale spunbonder

Experiments were carried out using a custom-built lab-scale spunbonding system at the Microcellular Plastics Manufac-turing Laboratory (MPML) at the University of Toronto. The machine features a circular spinneret die (see Figure 1) and a rectangular drafter inlet (see Figure 5) enclosed by side walls.

To validate the airflow simulations, air velocities were measured using an AVbase Dwyer pitot anemometer/manometer (Dwyer Instruments, LLC, Michigan City, IN, USA).

All trials used general-purpose PP H521 (Braskem America, Inc., Philadelphia, PA, USA). The extruder is equipped with four independently heated zones. The first zone, near the feed hopper, was set to 190 ℃, while the remaining zones and the die were maintained at 200 ℃. The feed hopper, fan, and screw rotation were each controlled via inverters. The feed rate exhibited a quasi-linear relationship with inverter frequency and was maintained within a range of 1-2 kg/h, allowing for continuous melt flow through all 100 circular die holes without interruptions or breakups.

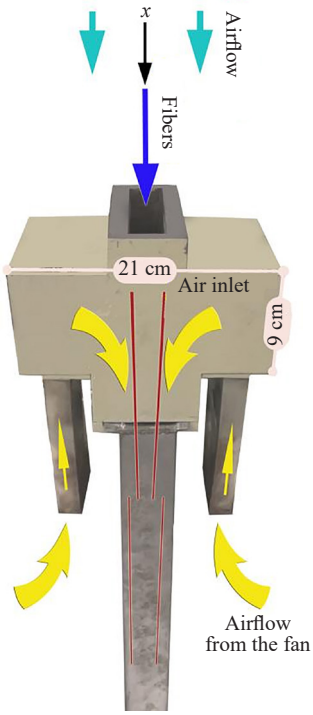

Figure 5. The drafter and air inlet configuration. A fan is controlled by an inverter and drives air into the drafter side inlets. Ambient air and polymer fibers enter from the top through a rectangular opening

The drafter fan was operated at two primary inverter settings: half draw and full draw. Under the half draw condition, the fan speed was set just high enough to maintain fiber alignment within the spinning path and prevent fibers from diverging toward the side walls. The corresponding air inlet velocity was measured to be approximately 50 m/s. In the full draw condition, the fan operated at the maximum speed that still ensured fiber continuity without breakage, resulting in an inlet velocity of 80 m/s. Due to the narrow drafter channel and enclosing side walls, velocity measurements were limited to the main air inlet and two additional accessible points along the flow path.

To sample fibers at specific locations along the drawing region, Liquid Nitrogen (LN_2) was used for rapid quenching. As shown in Figure 6, two thick metal plates cooled in LN_2 were used to freeze fibers at selected x-positions with minimal applied force, thereby preserving the fiber internal crystalline structure. There is a 50 cm distance below the die before the covering walls. We collected samples along this part and on the conveyor, where access was available, i.e., at x = 10, 20, 30, 50, and 220 cm below the die.

Fiber diameter measurements were performed using a 1,600 × Wendry Digital Electron Microscope (B0813J4TKF, manufactured in Shenzhen, Guangdong, China). Images were captured on a square grid scale and analyzed using ImageJ software [67] (Version 1.54 p). The average fiber diameters were plotted against x to observe thinning behavior. Under most operating conditions, the majority of diameter reduction occurred before x = 50 cm, consistent with freezing points reported in the literature [18]; under insufficient drawing conditions, however, the freezing point shifts further downstream, as discussed in Section 4.

Because sampling was necessarily limited to discrete spatial locations and a finite number of fibers per location, the reported diameters and crystallinity values should be interpreted as representative averages rather than pointwise spinline-resolved quantities. Nevertheless, the observed trends along the spinline were highly reproducible across repeated trials at the same operating conditions, supporting the robustness of the experimental dataset.

X-Ray Diffraction (XRD) analysis was conducted using a Philips PW3710 X-ray Diffractometer to determine the degree of crystallinity and investigate potential orientation effects. Diffraction angles ranging from 5° to 50° were recorded at a scanning rate of 4.0° min^{-1} to analyze the intensity of crystalline planes and assess structural evolution.

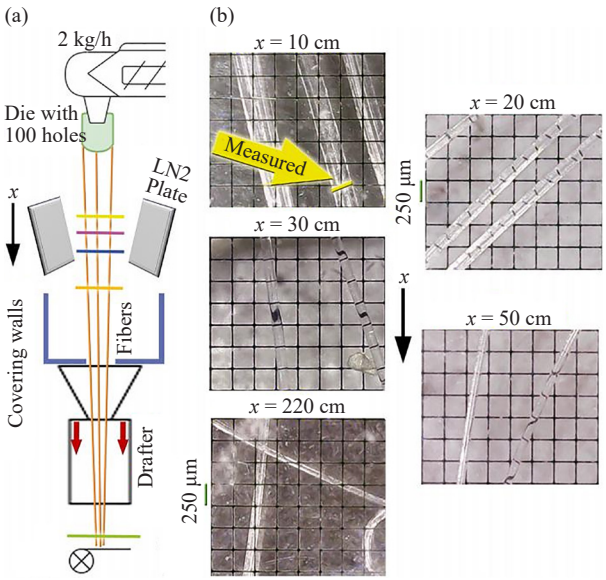

Figure 6. Collecting experimental data using LN_2. a) Metal plates were used to quench fiber samples at different positions. Three fibers are shown exiting the die and elongating through the drawing region. b) Optical microscope images of quenched samples, with a grid size of 250 µm, captured for the half draw condition. The five samples correspond to the five *x*-positions indicated in (a)

4. Results and discussion

We first present the simulation setup and results, then compare them with experimental measurements, and finally analyze the XRD data.

Figure 4 shows the main components of the spunbonding machine, including a schematic, the CAD geometry, the air inlets, and the three-dimensional CFD domain of the OpenFOAM mesh. The air inlet velocity was fixed to the measured values of 50 and 80 m/s for the half and full drawing settings, respectively. The velocity-driven air inlet boundaries, each about 2 cm horizontally from the spinline, draw ambient air through the top into the drafter, as illustrated in Figure 7a.

Figure 7b shows the resulting airflow along the spinline. U_a is negligible before the covering wall, where the fiber velocity is also minimal (i.e., x within 0 to 50 cm). Next, U_a gradually increases inside the covering walls from x = 50 to 100 cm before the drafter, and peaks in the upper half of the drafter, x = 100 to 150 cm. In the lower half of the drafter, U_a decreases due to air mixing and then increases again as the mixed air streams develop further downstream. The full and half draw settings exhibit similar qualitative patterns but differ in the magnitude of U_a, which affects the drag force. The profiles in Figure 7b were subsequently applied as boundary conditions to the fiber simulation.

We ran the 1D simulation based on Eq. (1) for ten values of G_K = 0 to 9, resulting in conveyor viscosities (η_{conveyor}) ranging from η_{die} to $\eta_{\text{die}} \times 10^5$. Figure 8 illustrates the viscosity increments using the empirical function of Eq. (8).

Once the operator identifies the closest match between the simulated and measured D_{conveyor}, the corresponding G_K is selected, and no further experimental measurements are required for that operating condition. Figure 9a illustrates how changes in G_K lead to a wide range of fiber diameters. The final diameter, D_{conveyor}, is particularly sensitive to crystallization and increases substantially as viscosity rises rapidly. This range is more clearly seen when comparing the velocity plots in Figure 9b. Note that the values of U are considerably smaller than U_a in Figure 7b.

Experiments described in Section 3 were conducted for different feed and draw settings. Four cases (two drawing settings and two feed rates) are shown in Figure 10. Each case corresponds to either the minimum or maximum draw and feed rates.

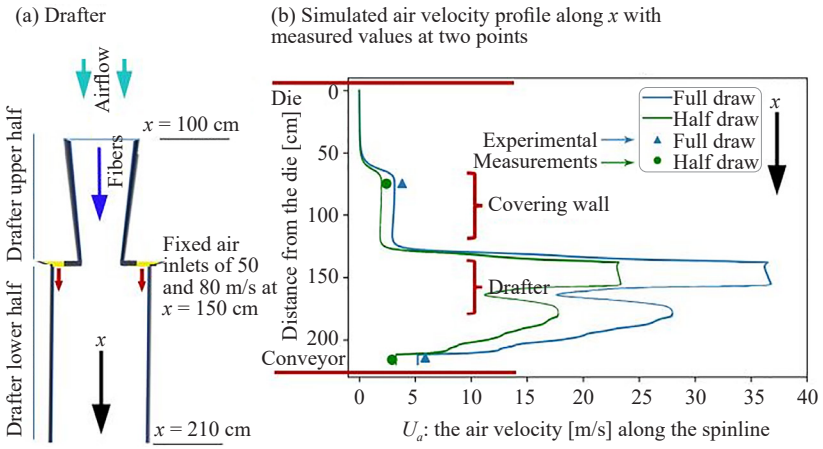

Figure 7. Simulation of U_a. a) A schematic of the upper and lower halves with the air inlet locations on the side walls. b) U_a profiles corresponding to full and half draw settings along the spinline from the die down to the belt. The measured velocities are as indicated

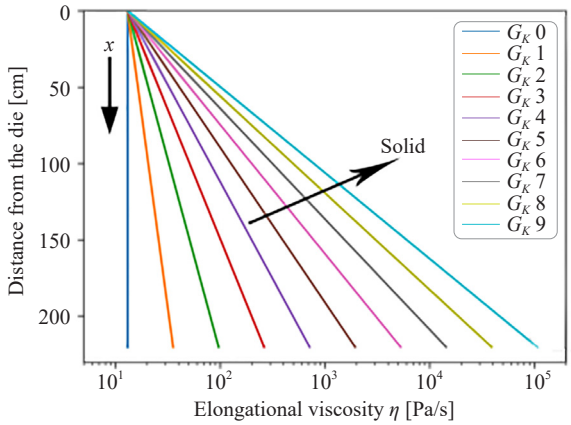

Figure 8. Elongational viscosity distribution along the spinline, x, for ten values of G_K = 0-9. G_K = 0 represents the limiting case of no crystallization

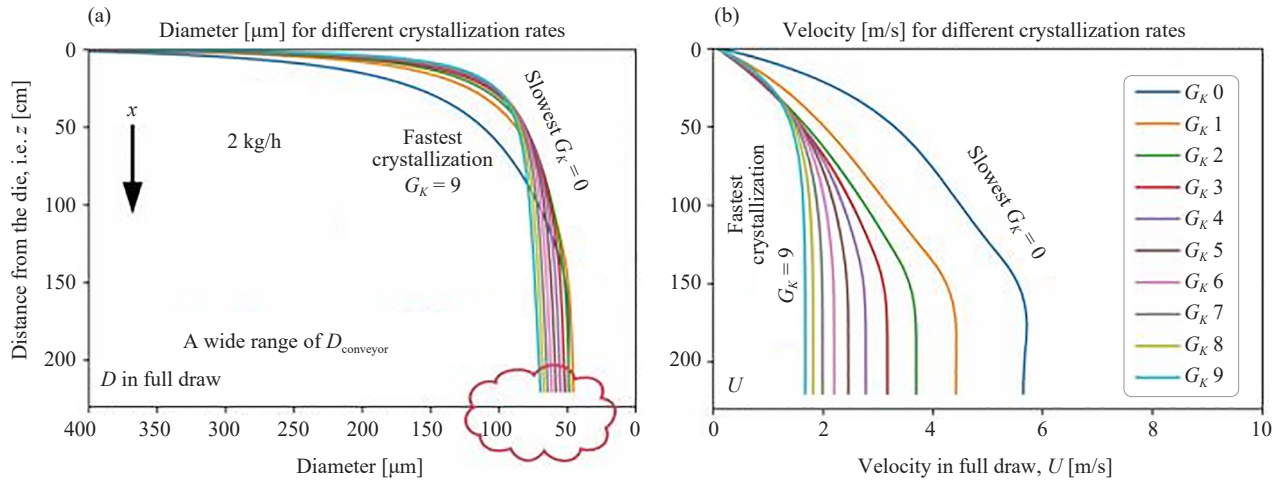

Figure 9. Distribution of a) fiber diameter, D, and b) fiber velocity, U, along the drawing region for G_K = 0-9 for a 2 kg/h feed rate. Note the wide variation in the final diameter, $D_{conveyor}$

The measured diameters are more scattered near the spinneret at higher feed rates, as shown in Figure 10c-d. One possible explanation is the emergence of variation between fibers located at the center and those near the edges of the die. Side fibers may experience higher drawing stress closer to the die due to their slightly smaller drawing angle—approximately 1°—from the circular die to the rectangular drafter. Although minor, this geometric deviation, coupled with increased exposure to the surrounding cooling air, may contribute to the observed diameter variation near the top of the spinline. Consequently, these measurements are not suitable for matching crystallization rates. By x = 220 cm, however, all fibers have sufficiently thinned, making the average diameter more representative.

Figure 11 compares experimental and simulated diameter profiles. Increasing the feed rate increases the final diameter due to reduced elongational stress and shorter residence time for thinning and crystallization. Similarly, lowering the draw increases fiber diameter by decreasing the shear drag. These trends are captured by the model.

An effective crystallization index of G_K = 6 yields the best agreement with experimental data at the lower feed rate of 1 kg/h, as evidenced by the blue and orange curves on the right-hand side of Figure 11. At this feed rate, the draw setting has only a minor effect on crystallization, primarily shifting the diameter profiles slightly to the left or right. In contrast, a value of G_K = 3 yields the best agreement at the higher feed rate of 2 kg/h under full draw. The fourth case, of a higher feed rate but only a half draw, leads to a noticeably larger final fiber diameter. In this case, we found that G_K = 0.5 yields the best agreement, suggesting that crystallization does not complete to the same extent under these conditions.

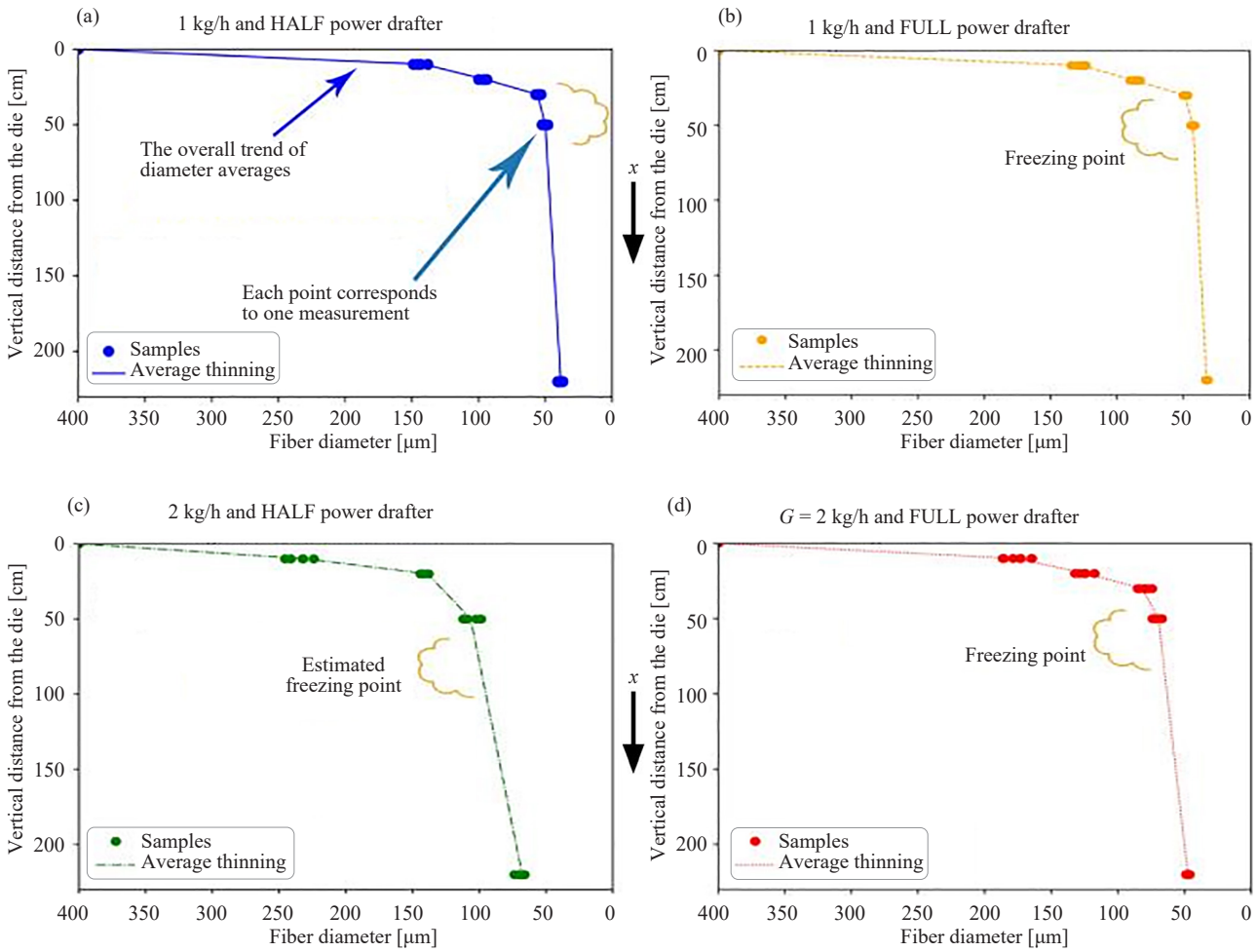

Figure 10. Experimental diameter trends along the spinline for four cases. a) 1 kg/h, half draw. b) 1 kg/h, full draw. c) 2 kg/h, half draw. d) 2 kg/h, full draw. Freezing points are marked

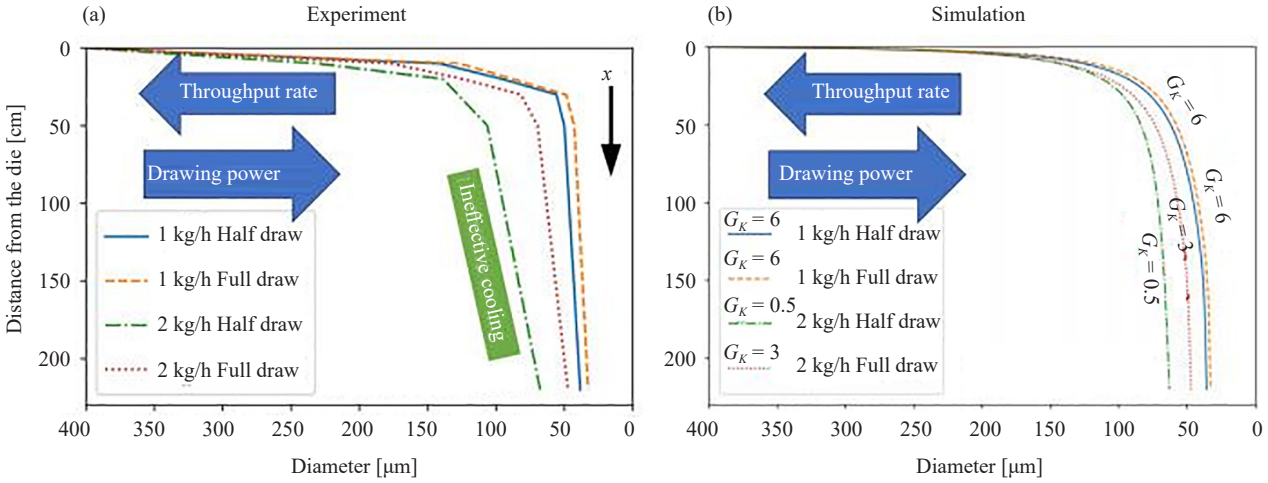

Figure 11. Comparison of fiber diameter distribution along the drawing region for four processing conditions: a) experi-mentally measured and b) simulated

The different G_K values at the high feed rate are primarily attributable to the limited time available for crystallization in the drawing region. Since the die hole diameter is fixed, increasing the feed rate to 2 kg/h approximately doubles the initial melt velocity, thereby reducing the residence time for thinning and crystallization before deposition. This results in a thicker fiber on the conveyor belt.

The simulation and experimental diameter profiles agree well across all four conditions, capturing both the qualitative trends and the quantitative thinning behavior along the spinline using a single fitted parameter per regime. The one notable exception is the case of a high feed rate at half draw, which represents a borderline operational limit where the polymer melt crystallizes too far downstream. Under these conditions, the drawing force is barely sufficient to complete crystallization, whereas the simulation assumes effective crystallization along the spinline. This mismatch suggests insufficient cooling capacity at this throughput level, and the operator must either increase the drawing force or reduce the feed rate. In our experiments, the high feed rate with half draw represented the lower limit of viable spunbonding operation. This case therefore defines one boundary of the model's validity domain: the 1D framework is applicable when the drawing force is sufficient to complete crystallization within the spinline.

To quantify this validity boundary, we introduce a Deborah number for crystallization:

$$De = \frac{\tau_{\text{crystal}}}{\tau_{\text{flow}}}. \tag{12}$$

where τ_{crystal} is the time the fiber spends within the crystallization temperature window ($T_g \leq T \leq T_m$, here 50-171 °C), and τ_{flow} is the total fiber residence time from die to conveyor. When $De \ll 1$, crystallization is confined to a small fraction of the spinline and the thermally dominated quasi-steady model is valid. As $De \rightarrow 1$, crystallization spans the full spinline and the separation of thermal and mechanical timescales breaks down.

Estimating these timescales from the cooling profiles and mass-conservation velocity fields for each experimental con-dition, we obtain $De \approx 0.15$-0.20 for the 1 kg/h cases: the higher velocity produces rapid cooling, so the crystallization window closes by $x \approx 37$ cm, well before the drafter entrance. The 2 kg/h full-draw condition yields $De \approx 0.30$, reflecting the slower cooling but still-adequate drawing force. The borderline condition—2 kg/h at half draw—produces $De \approx 0.8$: the XRD data in Section 4.1 confirm that crystallinity reaches $\xi = 0.96$ only at $x = 50$ cm (sample iv), meaning the crystallization window extends over the majority of the spinline. At this operating point, De approaches unity and the model operates at its limit, consistent with the observed mismatch in Figure 11. All other conditions tested in this work satisfy $De < 0.5$, confirming that the thermally dominated framework is justified for routine spunbonding operation.

4.1 *XRD analysis*

To further interpret the differences in G_K across operating conditions, we examine the crystalline structure of the LN_2-quenched samples using X-ray diffraction. Because the fibers were rapidly solidified, their crystalline structure reflects the extent of molecular alignment at each spinline position, providing a direct microscale correlate to the macroscopic G_K values. The 2 kg/h feed condition proved particularly informative, especially under half draw settings where crystallization occurs further along the spinline.

Table 2. Selected experimental data acquired from the XRD analysis summarize in Table 2 the intensity of the crystalline phases in specific directions. The total areas under the curves provide the crystallinity data, and the peaks indicate the intensity of directional growth and thus FIC and G_K. The selected samples correspond to Figure 12

Sample				(110)		(040)		(130)		(111)/(131)		$\xi^{[1]}$	G_K
#	kg/h	Draw	x [cm]	Area	2θ	Area	2θ	Area	2θ	Area	2θ	[__]	[__]
i	1	Half	20	0.24	14.8	0.25	17.3	0.11	19.2	0.21	22.1	0.68	6
ii	2	Half	20	0.22	14.2	0.43	16.4	0.11	17.0	0.07	18.8	0.55	0.5
iii	2	Full	20	0.18	14.8	0.19	17.4	0.11	19.1	0.27	22.1	0.59	3
iv	2	Half	50	0.16	14.6	0.25	17.4	0.12	19.3	0.22	22.2	0.96	0.5
v	2	Half	220	0.18	14.7	0.23	17.2	0.11	19.2	0.25	22.0	1.00	0.5

[1]The relative crystallinities were calculated from the XRD curves

The data in Table 2 for four cases (two drawing settings and two feed rates) provide key insights, such as the area under the curve for each peak, corresponding to the diffraction intensity from each crystallographic plane. These planes are also highlighted in Figure 12, which visually compares selected samples listed in the rows of Table 2, shown side by side for clearer assessment. The peak position indicates the diffraction angle (2θ) corresponding to each plane.

Figure 12a compares the XRD peaks of fibers collected 20 cm below the die at feed rates of 1 and 2 kg/h under half draw, corresponding to rows i and ii in Table 2. The diffraction peaks shift to smaller angles with increasing feed rate, indicating an expansion of the crystal unit cell size and a less densely packed crystalline structure. This behavior is consistent with weaker convective cooling and reduced extensional stress at the higher feed rate.

This trend is confirmed by the considerably higher $\xi = 0.68$ for the lower feed rate, consistent with the corresponding higher G_K. Notably, at 2 kg/h, fibers in case iii reach the same value of ξ of ii at higher x (i.e., further downstream), which is consistent with the difference between the corresponding G_K values.

Figure 12b presents diffraction patterns for samples collected 20 cm below the die, at 2 kg/h feed rate, comparing crystallization behavior under half draw versus full draw conditions. As supported by rows ii and iii in Table 2, the diffraction peaks at full draw shift to higher angles, while the areas under the large-angle peaks increase relative to the small-angle peaks. This indicates a more densely packed crystalline structure with preferred orientation along the direction normal to the (130) and (111)/(131) planes, consistent with stronger extensional deformation.

Figure 12c compares the diffraction peaks for fibers collected before the drafter at two distances from the die at 2 kg/h. As evident from rows ii and iv in Table 2, fibers collected further from the die exhibit diffraction peaks shifted to larger angles and a relative increase in the area under the large-angle peaks. This trend indicates a more closely packed crystalline structure with preferred orientation as the fiber progresses down the spinline, consistent with increasing chain alignment.

Figure 12d compares the diffraction peaks for fiber samples collected above the drafter to those on the conveyor belt. The relative areas under all peaks remain approximately constant. This trend is also reflected in rows iv and v of Table 2. No significant peak shifts are observed when comparing the two spectra, indicating minimal distortion in the crystal unit cell and no substantial enhancement in crystal packing from 50 cm down the spinline to the conveyor belt. This observation is consistent with the simulation results, where fiber diameter from immediately before the drafter to the conveyor belt does not change appreciably.

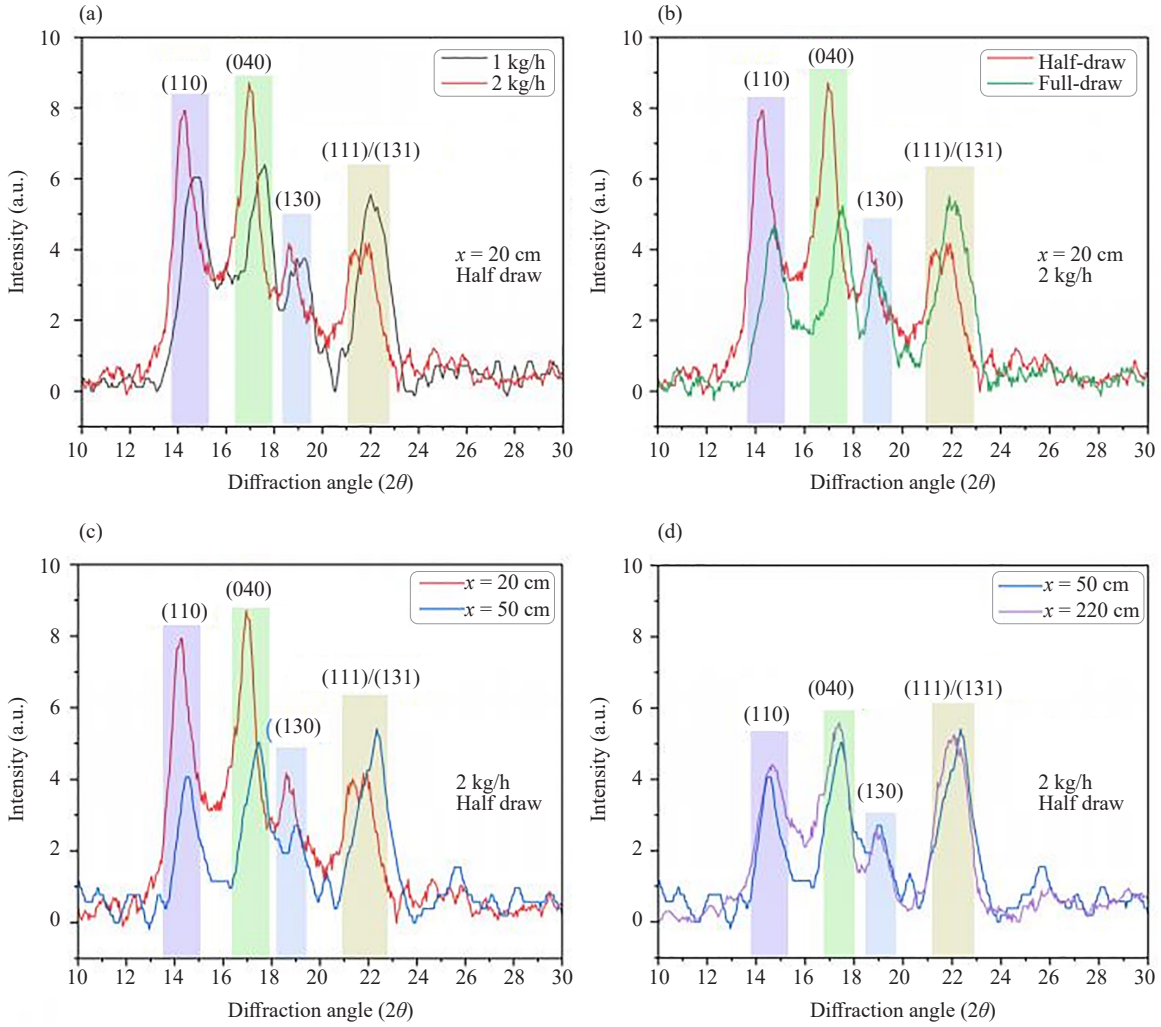

Figure 12. XRD analysis of PP samples from our custom-made spunbonding machine. Comparisons of the diffraction patterns are shown for a) high and low feed rates at x = 20 cm at half draw, b) half and full draw at x = 20 cm and high feed rate, c) x = 20 and 50 cm at half draw and high feed rate, and d) x = 50 and 220 cm at half draw and high feed rate

As evident in Figure 12b, the XRD peaks shift to higher angles with higher drawing force, and the higher angle peaks increase in area, similar to the behavior observed in Figure 12a for different feed rates. This indicates a more densely packed crystalline structure with stronger preferred orientation, consistent with the higher extensional stresses under full draw. However, G_K captures an effective crystallization rate based on relative crystallinity rather than an absolute rate. An increase in fiber velocity can partially compensate for a faster absolute crystallization rate, yielding a similar relative crystallinity. This explains why increasing drafter power, despite raising the absolute crystallization rate, produces finer fibers, as seen in both the simulation and experimental results in Figure 11.

Finally, the significant difference in relative crystallinity between rows i and ii highlights the substantial difference in fitted G_K values for feed rates of 1 and 2 kg/h. Additionally, the ξ value for row iii is slightly higher than that of ii, which is consistent with the prediction for the same G_K. The value ξ = 0.96 for sample iv indicates that the freezing point occurred within the physically accessible range of our experiment.

The fitted G_K values are directly reflected in the quantitative crystallinity data. At 1 kg/h (row i, G_K = 6), the relative crystallinity at x = 20 cm reaches ξ = 0.68—significantly higher than ξ = 0.55 measured at the same location for 2 kg/h half-draw (row ii, G_K = 0.5). This is physically consistent: the lower feed rate produces a slower-moving fiber that accumulates greater crystallization driving force, which is captured by the higher G_K. The 2 kg/h full-draw case (row iii, G_K = 3) yields an intermediate ξ = 0.59, reflecting the higher draw force that promotes faster crystallization

relative to the half-draw case. The XRD peak distributions corroborate this hierarchy: conditions with higher G_K exhibit stronger orientation peaks and denser crystalline packing, consistent with enhanced molecular alignment under greater extensional stress. A fully quantitative relationship between G_K and specific microstructural metrics—such as orientation index, peak intensity ratio, or crystallite size—would require coordinated process–XRD measurements and is identified as a valuable direction for future work.

Regarding crystal polymorph identification and crystallite dimensions: the dominant 2θ peaks across all samples are consistent exclusively with the α-monoclinic form of isotactic PP; no reflection near 16.2° attributable to the β-trigonal polymorph was detected in any sample. Crystallite dimensions were estimated from Gaussian fits to the raw diffraction profiles using the Scherrer equation $D_{hkl} = K\lambda/(\beta \cos\theta)$ with $K = 0.9$ and $\lambda = 1.5406$ ($Cu\ K_{\alpha 1}$). The (110) reflection—resolved in all five samples at $2\theta \approx 14.3$-$14.7°$—yields crystallite dimensions of approximately 6.1, 6.9, 6.7, 7.8, and 6.1nm for rows i through v, respectively; this narrow range (6-8 nm) shows no systematic dependence on processing condition or G_K, indicating that the unit-cell packing of the α-PP crystallites is governed primarily by thermodynamics rather than by the kinetic parameter G_K. The 2 kg/h half-draw sample at $x = 20$ cm (row ii) exhibits the most fully resolved α-PP diffraction pattern, with the (040) and (130) reflections clearly separated alongside the (110) peak, consistent with a higher degree of long-range crystalline order at that location.

5. Conclusion

A 1D fiber formation model for the spunbonding drawing region has been developed, shifting modeling complexity from the crystallizing melt to the airflow field. The model predicts fiber diameter evolution under varying feed rates and draw conditions using a single empirical parameter, G_K, together with a simplified combined equation for rheology and crystallization. G_K is not a material constant but a system-dependent effective parameter, defined as the logarithm of the total viscosity amplification from die to conveyor, $G_K = \ln(\eta_{\text{conveyor}}/\eta_{\text{die}})$; its value varies with throughput and drawing conditions but remains fixed once identified for a given operating regime. It is applicable to different spunbonding machine geometries, provided that the material properties at the die are known and the air velocity profile U_a is available either from CFD simulation or from direct measurement at several points along the drawing region. This makes the framework practical for routine process adjustments such as feed rate changes, material grade variations, or drafter airflow tuning.

Experimental validation confirms the assumption of negligible induction time and justifies the simplifications adopted in the momentum and energy equations for thin spunbonded fibers. The thermally dominated crystallization formulation— in which $\xi(T)$ depends on temperature alone while flow-induced crystallization effects are captured indirectly through G_K—represents a deliberate simplification that is confirmed adequate by the model's good agreement with experimental data across all tested conditions. The XRD results further elucidate the crystalline structure and show that variations in the fitted values of G_K represent differences in crystallization extent and crystal orientation. The present 1D framework does not capture radial distributions such as skin-core morphology [60], [61]; this represents a limitation to be addressed in future work.

The agreement between simulations and experiments across multiple feed and draw conditions confirms that the model serves as a reliable reduced-order framework for interpreting fiber thinning and effective crystallization behavior in spunbonding, with practical utility for process tuning at the industrial scale.

Acknowledgment

We appreciate the funding and support from the Ministry of Trade, Industry & Energy (MOTIE), Korea, which made this study possible. All computations were performed on the Niagara supercomputer of the Digital Research Alliance of Canada, the Ontario Research Fund: Research Excellence, and the University of Toronto.

Co-author contributions

Co-author contributions for Behrang Mohajer: Conceptualization, Methodology, Investigation, Software, Val-idation, Formal analysis, Writing -Original Draft, Visualization. Amirmehdi Salehi and Amirjalal Jalali: Val-idation, Investigation, and Formal analysis. Markus Bussmann and Chul B. Park: Conceptualization, Formal analysis, Resources, Writing -Review & Editing, Supervision, Project administration, Funding acquisition.

Funding

This work was financially supported by the Technology Innovation Program (or Industrial Strategic Tech-nology Development Program) (RS-2024-00433288) funded by the Ministry of Trade, Industry & Energy (MOTIE), Korea.

Research data statement

The experimental data will be available upon request.

Declaration of generative AI and AI-assisted technologies

During the preparation of this work, the authors used ChatGPT only to improve the English for some paragraphs. After using these services, the authors reviewed and edited the content as needed and take full responsibility for the content of the published article.

Conflicts of interest

The authors declare no competing financial interest.

References

[1] K. G. Allison, "Process for forming non-woven filamentary structures from fiber-forming synthetic organic polymers," U. S. Patent 3,338,992, 29 Aug., 1967.

[2] S. Kase and T. Matsuo, "Studies on melt spinning. I. Fundamental equations on the dynamics of melt spinning," *Journal of Polymer Science Part A: General Papers*, vol. 3, no. 7, pp. 2541-2554, 1965.

[3] V. Bansal and R. L. Shambaugh, "On-line determination of density and crystallinity during melt spinning," *Polymer Engineering & Science*, vol. 36, no. 22, pp. 2785-2798, 1996.

[4] A. K. Doufas, I. S. Dairanieh, and A. J. McHugh, "A continuum model for flow-induced crystallization of polymer melts," *Journal of Rheology*, vol. 43, no. 1, pp. 85-109, 1999.

[5] A. Yarin, S. Sinha-Ray, and B. Pourdeyhimi, "Meltblowing: Multiple polymer jets and fiber-size distribution and lay-down patterns," *Polymer*, vol. 52, no. 13, pp. 2929-2938, 2011.

[6] Y. Pu, J. Zheng, F. Chen, Y. Long, H. Wu, Q. Li, S. Yu, X. Wang, and X. Ning, "Preparation of polypropylene micro and nanofibers by electrostatic-assisted melt blown and their application," *Polymers*, vol. 10, no. 9, pp. 959, 2018.

[7] G. Sun, Y. Ruan, X. Wang, S. Xin, Y. Chen, and W. Hu, "Numerical study of melt-blown fibrous web uniformity based on the fiber dynamics on a collector," *Industrial & Engineering Chemistry Research*, vol. 58, no. 51, pp. 23519-23528, 2019.

[8] A. Ghosal, K. Chen, S. Sinha-Ray, A. L. Yarin, and B. Pourdeyhimi, "Modeling polymer crystallization kinetics in the meltblowing process," *Industrial & Engineering Chemistry Research*, vol. 59, no. 1, pp. 399-412, 2019.

[9] A. Rizvi, Z. K. Andalib, and C. B. Park, "Fiber-spun polypropylene/polyethylene terephthalate microfibrillar

composites with enhanced tensile and rheological properties and foaming ability," *Polymer*, vol. 110, pp. 139-148, 2017.
[10] C. Zhao, L. H. Mark, M. Alshrah, I. Soltani, P. C. Lee, and C. B. Park, "Challenge in manufacturing nanofibril composites with low matrix viscosity: Effects of matrix viscosity and fibril content," *European Polymer Journal*, vol. 121, pp. 109310, 2019.
[11] I. Soltani, L. H. Mark, A. Jalali, H. Akrami, C. Zhao, M. R. Saeb, and C. B. Park, "Optimization of manufacturing process for nanofibrillated spunbond composite products," *Journal of Manufacturing Processes*, vol. 120, pp. 680-693, 2024.
[12] Z. Ke, L. Yu, G. Wang, R. Sun, M. Zhu, H. Dong, Y. Xu, M. Ren, S. Fu, and C. Zhi, "Three-dimensional modeling of spun-bonded nonwoven meso-structures," *Polymers*, vol. 15, no. 3, pp. 600, 2023.
[13] R. I. Tanner and F. Qi, "Stretching, shearing and solidification," *Chemical Engineering Science*, vol. 64, no. 22, pp. 4576-4579, 2009.
[14] M. Derakhshandeh and S. G. Hatzikiriakos, "Flow-induced crystallization of high-density polyethylene: The effects of shear and uniaxial extension," *Rheologica Acta*, vol. 51, pp. 315-327, 2012.
[15] A. Rawal and S. Mukhopadhyay, "4-Melt spinning of synthetic polymeric filaments," in *Advances in Filament Yarn Spinning of Textiles and Polymers*, D. Zhang, Ed. United Kingdom: Woodhead Publishing, 2014, pp. 75-99.
[16] G. S. Bhat and S. R. Malkan, "Extruded continuous filament nonwovens: Advances in scientific aspects," *Journal of Applied Polymer Science*, vol. 83, no. 3, pp. 572-585, 2001.
[17] R. Beyreuther and H. Brünig, *Dynamics of Fibre Formation and Processing: Modelling and Application in Fibre and Textile Industry*. Heidelberg: Springer, 2006.
[18] E. B. Bond, "Ziegler-Natta and metallocene-catalyzed isotactic polypropylene: A comprehensive investigation and comparison using crystallization kinetics, fiber spinning and thermal spunbonding". Ph. D. dissertation, The University of Tennessee, Knoxville, TN, USA, 1999.
[19] A. K. Doufas, A. J. McHugh, C. Miller, and A. Immaneni, "Simulation of melt spinning including flow-induced crystallization: Part II. Quantitative comparisons with industrial spinline data," *Journal of Non-Newtonian Fluid Mechanics*, vol. 92, no. 1, pp. 81-103, 2000.
[20] A. Ziabicki and L. Jarecki, "Crystallization-controlled limitations of melt spinning," *Journal of Applied Polymer Science*, vol. 105, no. 1, pp. 215-223, 2007.
[21] T. Chen, X. Wang, and X. Huang, "Modeling the air-jet flow field of a dual slot die in the melt blowing nonwoven process," *Textile Research Journal*, vol. 74, no. 11, pp. 1018-1024, 2004.
[22] J. H. Beard, R. L. Shambaugh, B. R. Shambaugh, and D. W. Schmidtke, "On-line measurement of fiber motion during melt blowing," *Industrial & Engineering Chemistry Research*, vol. 46, no. 22, pp. 7340-7352, 2007.
[23] A. Grice, "Modelling the creation of polymer fibres for nonwoven fabrics," Ph. D. thesis, Loughborough University, Loughborough, U. K., 2018.
[24] G. Sun, J. Yang, S. Xin, R. Yu, and X. Wang, "Influence of processing conditions on the basis weight uniformity of melt-blown fibrous webs: Numerical and experimental study," *Industrial & Engineering Chemistry Research*, vol. 57, no. 29, pp. 9707-9715, 2018.
[25] O. L. Shealy, "Spunbonded products—a new concept in utilization of fibrous materials," *Textile Research Journal*, vol. 35, no. 4, pp. 322-329, 1965.
[26] L. Hosun, "A review of spun bond process," *Journal of Textile and Apparel, Technology and Management*, vol. 6, no. 3, pp. 1-13, 2010.
[27] B. Zhao, "Numerical simulation and experimental study of the polypropylene polymer air drawing model and air jet flow field model in the spunbonding nonwoven process," *Industrial & Engineering Chemistry Research*, vol. 52, no. 32, pp. 11061-11069, 2013.
[28] T. Kanai, Y. Kohri, and T. Takebe, "Theoretical analysis of the spunbond process and its applications for polypropylenes," *Advances in Polymer Technology*, vol. 37, no. 6, pp. 2085-2094, 2018.
[29] K. Chen, A. Ghosal, A. L. Yarin, and B. Pourdeyhimi, "Modeling of spunbond formation process of polymer nonwovens," *Polymer*, vol. 187, pp. 121902, 2020.
[30] T. Chen, C. Zhang, L. Li, and X. Chen, "Simulating the drawing of spunbonding nonwoven process using an artificial neural network technique," *Journal of the Textile Institute*, vol. 99, no. 5, pp. 479-488, 2008.
[31] B. Zhao, "Predicting the fiber diameter of spunbonding nonwovens fabrics by means of physical model, statistical method and artifical neural network theory," *International Journal of Clothing Science and Technology*, vol. 27, no. 2, pp. 262-271, 2015.
[32] S. Gramsch, A. Sarishvili, and A. Schmeißer, "Analysis of the fiber laydown quality in spunbond processes with

simulation experiments evaluated by blocked neural networks," *Advances in Polymer Technology*, vol. 2020, pp. 1-11, 2020.
[33] B. Mohajer, A. Salehi, M. Kheradmandkeysomi, A. Jalali, M. Bussmann, and C. B. Park, "Choice of the mathematical models in the simulation of elongational flow-induced crystallization (FIC) during polymer processing: A review," *Thermal Science and Applications*, vol. 1, no. 1, pp. 65-91, 2026.
[34] Y. Nie, J. Wen, Y. Ming, and Y. Zhou, "Mechanisms of flow-induced multistep structure evolution in semicrystalline polymers revealed by molecular simulations," *Crystal Growth & Design*, vol. 24, no. 15, pp. 6531-6547, 2024.
[35] R. Spina, M. Spekowius, and C. Hopmann, "Multiphysics simulation of thermoplastic polymer crystallization," *Materials & Design*, vol. 95, pp. 455-469, 2016.
[36] R. Arrigo, G. Malucelli, and F. P. L. Mantia, "Effect of the elongational flow on the morphology and properties of polymer systems: A brief review," *Polymers*, vol. 13, no. 20, pp. 3529, 2021.
[37] M. Chellamuthu, D. Arora, H. H. Winter, and J. P. Rothstein, "Extensional flow-induced crystallization of isotactic poly-1-butene using a filament stretching rheometer," *Journal of Rheology*, vol. 55, no. 4, pp. 901-920, 2011.
[38] A. Salehi, M. Kheradmandkeysomi, S. S. Rahman, R. Rahmati, A. Afzal, R. Li, and C. B. Park, "Fabricating super-tough polypropylene nanocomposites incorporating silane cross-linked in-situ nano-fibrillated ethylene-1-butene copolymer," *Materials Today Chemistry*, vol. 35, pp. 101856, 2024.
[39] M. Kheradmandkeysomi, A. Salehi, A. Jalali, H. Omranpour, O. A. Tafreshi, H. E. Naguib, and C. B. Park, "Enhancing mechanical performance of high-density polyethylene at different environmental conditions with outstanding foamability through in-situ rubber nanofibrillation: Exploring the impact of interface modification," *ACS Applied Materials & Interfaces*, vol. 16, no. 22, pp. 29291-29304, 2024.
[40] B. Chang, K. Schneider, R. Vogel, and G. Heinrich, "Influence of nucleating agent self-assembly on structural evolution of isotactic polypropylene during uniaxial stretching," *Polymer*, vol. 138, pp. 329-342, 2018.
[41] K. Jayanarayanan, T. Jose, S. Thomas, and K. Joseph, "Effect of draw ratio on the microstructure, thermal, tensile and dynamic rheological properties of insitu microfibrillar composites," *European Polymer Journal*, vol. 45, no. 6, pp. 1738-1747, 2009.
[42] H. Wang, X. Jin, N. Mao, and S. J. Russell, "Differences in the tensile properties and failure mechanism of PP/PE core/sheath bicomponent and PP spunbond fabrics in uniaxial conditions," *Textile Research Journal*, vol. 80, no. 17, pp. 1759-1767, 2010.
[43] S. A. Arvidson, K. C. Wong, R. E. Gorga, and S. A. Khan, "Structure, molecular orientation, and resultant mechanical properties in core/sheath poly (lactic acid)/polypropylene composites," *Polymer*, vol. 53, no. 3, pp. 791-800, 2012.
[44] A. Anstey, A. V. Tuccitto, P. C. Lee, and C. B. Park, "Generation of tough, stiff polylactide nanocomposites through the in situ nanofibrillation of thermoplastic elastomer," *ACS Applied Materials & Interfaces*, vol. 14, no. 12, pp. 14422-14434, 2022.
[45] A. Jalali, S. Romero-Diez, M. Nofar, and C. B. Park, "Entirely environment-friendly polylactide composites with outstanding heat resistance and superior mechanical performance fabricated by spunbond technology: Exploring the role of nanofibrillated stereocomplex polylactide crystals," *International Journal of Biological Macromolecules*, vol. 193, pp. 2210-2220, 2021.
[46] M. Kheradmandkeysomi, A. Salehi, A. Jalali, H. Akrami, and C. B. Park, "Achieving super-tough high-density polyethylene with promising foamability using silane crosslinked polyolefin elastomer nanofibrils network," *Composites Science & Technology*, vol. 251, pp. 110576, 2024.
[47] V. K. Konaganti, M. Derakhshandeh, M. Ebrahimi, E. Mitsoulis, and S. G. Hatzikiriakos, "Non-isothermal extrudate swell," *Physics of Fluids*, vol. 28, no. 12, pp. 123101, 2016.
[48] N. H. A. Tran, H. Brünig, R. Boldt, and G. Heinrich, "Morphology development from rod-like to nanofibrillar structures of dispersed poly (lactic acid) phase in a binary blend with poly (vinyl alcohol) matrix along the spinline," *Polymer*, vol. 55, no. 24, pp. 6354-6363, 2014.
[49] A. K. Doufas, A. J. McHugh, and C. Miller, "Simulation of melt spinning including flow-induced crystallization Part I. Model development and predictions," *Journal of Non-Newtonian Fluid Mechanics*, vol. 92, no. 1, pp. 27-66, 2000.
[50] S. K. Batra and B. Pourdeyhimi, *Introduction to Nonwovens Technology*. DEStech Publications, Inc, 2012.
[51] B. Zhao, "Modeling polypropylene polymer air drawing in the spunbonding nonwoven process," *International Journal of Clothing Science and Technology*, vol. 26, no. 2, pp. 184-194, 2014.
[52] S. Acierno, S. Coppola, N. Grizzuti, and P. L. Maffettone, "Coupling between kinetics and rheological parameters in the flow-induced crystallization of thermoplastic polymers," *Macromolecular Symposia*, vol. 185, no. 1, pp.

233-241, 2002.
[53] K. H. Kim, A. Isayev, and K. Kwon, "Flow-induced crystallization in the injection molding of polymers: A thermodynamic approach," *Journal of Applied Polymer Science*, vol. 95, no. 3, pp. 502-523, 2005.
[54] Y. Rong, H. He, W. Cao, C. Shen, and J. Chen, "Multi-scale molding and numerical simulation of the flow-induced crystallization of polymer," *Computational Materials Science*, vol. 67, pp. 35-39, 2013.
[55] R. Spina, M. Spekowius, and C. Hopmann, "Multi-scale thermal simulation of polymer crystallization," *International Journal of Material Forming*, vol. 8, pp. 497-504, 2015.
[56] A. Ghosal, S. Sinha-Ray, A. L. Yarin, and B. Pourdeyhimi, "Numerical prediction of the effect of uptake velocity on three-dimensional structure, porosity and permeability of meltblown nonwoven laydown," *Polymer*, vol. 85, pp. 19-27, 2016.
[57] B. Mohajer, M. Kheradmandkeysomi, S. Amirzadeh, M. Bussmann, and C. B. Park, "Simplified dual-scale simulation framework for computational modeling of nanofibrillation phenomena via fiber in fiber technology with experimental data," *Engineering with Computers*, vol. 42, no. 2, pp. 44, 2026.
[58] H. G. Weller, G. Tabor, H. Jasak, and C. Fureby, "A tensorial approach to computational continuum mechanics using object-oriented techniques," *Computers in Physics*, vol. 12, no. 6, pp. 620-631, 1998.
[59] B. Mohajer, M. Kheradmandkeysomi, C. B. Park, and M. Bussmann, "Enhancing drafter performance in spunbonding of polymeric fibers via airflow simulation," *Polymers*, vol. 18, no. 2, pp. 187, 2026.
[60] D. Pan, H. He, J. Sun, M. Cao, Z. Qin, and L. Chen, "Radial crystallization difference of melt-spun polypropylene fiber along spinning line," *Journal of Applied Polymer Science*, vol. 136, no. 11, pp. 47175, 2019.
[61] M. Müller, C. Riekel, R. Vuong, and H. Chanzy, "Skin/core micro-structure in viscose rayon fibres analysed by x-ray microbeam and electron diffraction mapping," *Polymer*, vol. 41, no. 7, pp. 2627-2632, 2000.
[62] C. H. Chen, J. L. White, J. E. Spruiell, and B. C. Goswami, "Dynamics, air drag, and orientation development in the spunbonding process for nonwoven fabrics," Textile Research Journal, vol. 53, no. 1, pp. 44-51, 1983.
[63] F. Pimenta and M. A. Alves, "Stabilization of an open-source finite-volume solver for viscoelastic fluid flows," *Journal of Non-Newtonian Fluid Mechanics*, vol. 239, pp. 85-104, 2017.
[64] A. Ziabicki and P. Sajkiewicz, "Crystallization of polymers in variable external conditions. III: Experimental determination of kinetic characteristics," *Colloid & Polymer Science*, vol. 276, pp. 680-689, 1998.
[65] A. Ziabicki, "Crystallization of polymers in variable external conditions: II. effects of cooling in the absence of stress and orientation," *Colloid & Polymer Science*, vol. 274, pp. 705-716, 1996.
[66] A. Ziabicki, "Crystallization of polymers in variable external conditions iv. isothermal crystallization in the presence of variable tensile stress or hydrostatic pressure," *Colloid and Polymer Science*, vol. 277, pp. 752-761, 1999.
[67] J. Schindelin, I. Arganda-Carreras, E. Frise, V. Kaynig, M. Longair, T. Pietzsch, S. Preibisch, C. Rueden, S. Saalfeld, B. Schmid, et al., "Fiji: An open-source platform for biological-image analysis," *Nature Methods*, vol. 9, no. 7, pp. 676-682, 2012.